Li, S., Bedford, J., Moreno, M., Barnhart, W. D., Rosenau, M., Oncken, O. (2018): Spatiotemporal variation of mantle viscosity and the presence of cratonic mantle inferred from eight years of postseismic deformation following the 2010 Maule Chile earthquake. - *Geochemistry Geophysics Geosystems (G3)*, *19*, 9, pp. 3272—3285.

DOI: http://doi.org/10.1029/2018GC007645

AGU100 ADVANCING EARTH AND SPACE SCIENCE

Geochemistry, Geophysics, Geosystems

RESEARCH ARTICLE
10.1029/2018GC007645

Key Points:
- Eight years of continuous GPS observations following the 2010 Maule, Chile, earthquake show intriguing spatiotemporal deformation pattern
- In the proximal area, between 300 and 700 km from the trench, the viscosity is temperature and stress dependent inferred from modeling
- In the distal area, between 700 and ~1,400 km, a highly viscous cratonic mantle is inferred

Supporting Information:
- Supporting Information S1

Correspondence to:
S. Li,
shaoyang-li@uiowa.edu

Citation:
Li, S., Bedford, J., Moreno, M., Barnhart, W. D., Rosenau, M., & Oncken, O. (2018). Spatiotemporal variation of mantle viscosity and the presence of cratonic mantle inferred from 8 years of postseismic deformation following the 2010 Maule, Chile, earthquake. *Geochemistry, Geophysics, Geosystems*, *19*, 3272–3285. https://doi.org/10.1029/2018GC007645

Received 1 MAY 2018
Accepted 15 AUG 2018
Accepted article online 23 AUG 2018
Published online 19 SEP 2018

Spatiotemporal Variation of Mantle Viscosity and the Presence of Cratonic Mantle Inferred From 8 Years of Postseismic Deformation Following the 2010 Maule, Chile, Earthquake

Shaoyang Li[1,2], Jonathan Bedford[1], Marcos Moreno[1,3], William D. Barnhart[2], Matthias Rosenau[1], and Onno Oncken[1]

[1]Helmholtz Centre Potsdam, GFZ German Research Centre for Geosciences, Potsdam, Germany, [2]Department of Earth and Environmental Sciences, University of Iowa, Iowa City, IA, USA, [3]Department of Geophysics, University of Concepcion, Concepcion, Chile

Abstract Postseismic displacements following great subduction earthquakes show significant long-wavelength and time-dependent patterns caused primarily by transient viscoelastic relaxation processes occurring broadly at depth. However, the Earth's viscosity structure and time-dependent variations are still poorly understood, especially in the years immediately following a great earthquake. Here we investigate the spatiotemporal variation of mantle viscosity proximal and distal to the southern Andes using 8 years of continuous high-resolution GPS observations following the 2010 M_w 8.8 Maule earthquake in south Central Chile. We remove the potential influences of relocking and afterslip on far-field GPS displacements and estimate viscosities that can explain the 3-D displacements. The optimal viscosity structure exhibits a low-viscosity (~10^{18}Pa s) mantle beneath the Andean volcanic arc and high-viscosity (>10^{22}Pa s) cratonic mantle, indicating a dependence of transient viscosity on temperature. Comparisons of the viscosity distributions at different times show that mantle viscosities increase with time throughout the study region. Viscosity increase is generally fastest in the mantle wedge beneath the Andes and slows down with increasing distance from the source region of the Maule earthquake. Such temporal viscosity evolution may indicate a stress dependence of the viscosity proximal to the rupture zone, while regions east of the Andes act as a relatively rigid body (i.e., cratonic mantle) with much higher viscosity. Our results thus suggest that both temperature structure and stress state contribute to spatiotemporal variations of the mantle viscosity. Heterogeneous spatiotemporal variations of viscosity seem to control the expansion and duration of the postseismic deformation and therefore the postseismic stress evolution.

Plain Language Summary We used continuous GPS positioning data to study the viscosity distribution at depth and its time variation following the 2010 M_w 8.8 Maule, Chile, earthquake. We find that the viscosities in the volcanic/mountain range regions, where deep rocks are expected hot, are relatively low (i.e., the materials are in weak state prone to flow easily), while the viscosities in far regions, where an ancient cold crust is expected, are relatively high (i.e., the materials are too strong to flow). This finding can, therefore, be related to the temperature distribution at depth. Furthermore, we find that the viscosities in all regions except the region of ancient crust increase with time and the rate of viscosity recovery decreases with the distance to the earthquake location. This phenomenon can, therefore, be related to the earthquake-induced stresses. Another interesting thing found in this study is that the ancient crust is likely not influenced much by the earthquake and behaves very strong in all the observation time. In all, we propose that both temperature and earthquake stresses control the rock strengths following a great earthquake. This study thus contributes to our understanding of the stress evolution at depth through the earthquake cycle and hence mechanisms of the earthquake happening.

1. Introduction

Constraining the rock rheology of the asthenosphere on the continental scale is fundamentally important to our understanding of the evolution and dynamics of subduction zones and mountain belts (Burgmann & Dresen, 2008). When a megathrust fault interface fails coseismically in a sudden great event, it induces large stress perturbations in the surrounding lithosphere and asthenosphere. Such perturbations drive subsequent postseismic material flow (i.e., viscoelastic relaxation) at depth, relaxing the coseismic extension of the upper

plate and underlying mantle. Depending on the magnitude of the earthquake, postseismic relaxation may be reflected by centimeter- to meter-scale surface displacements over spatial scales of hundreds to thousands of kilometers and over timescales of years to decades.

Through numerical modeling, postseismic surface displacements measured by space geodesy (e.g., Global Positioning System [GPS] and interferometric synthetic aperture radar [InSAR]) can provide insights into the rheological structure and mechanical properties of the mantle (e.g., Freed et al., 2017; Hu et al., 2016; Li et al., 2017; Moore et al., 2017; Nur & Mavko, 1974; Wiseman et al., 2015). Recent postseismic studies of great subduction zone earthquakes (e.g., the 2004 M_w 9.2 Sumatra-Andaman earthquake, Wiseman et al., 2015; the 2010 M_w 8.8 Maule, Chile, earthquake, Klein et al., 2016; Li et al., 2017; and the 2011 M_w 9.1 Tohoku-oki, Japan, earthquake, Freed et al., 2017; Sun et al., 2014) suggest that the mantle viscosity structure is highly heterogeneous. These results are not unexpected given the lateral heterogeneities in both material properties and thermal conditions that are ubiquitous to convergent plate boundaries and subduction zones. Temporally variable viscosities have also been inferred from geodetic time series of postseismic relaxation (e.g., Freed & Burgmann, 2004; Hussain et al., 2018; Malservisi et al., 2015; Pollitz et al., 2001). A common and convenient approximation of the transient viscosity is the biviscous Burgers rheology, which allows for an initial short-term viscosity that transitions into a longer-term viscosity (e.g., Pollitz, 2003; Wang et al., 2012). Another commonly used rheology, physics-based power law rheology, allows for a continuous increase of viscosity constrained by laboratory-scale empirical relationships of stress dependency (e.g., Freed & Burgmann, 2004; Kirby & Kronenberg, 1987; Sobolev & Muldashev, 2017). These rheology models, though, include necessary simplifications or are based on empirical relationships. The first-order complexity of transient evolution of viscosity is necessarily constrained in the perspective of nature observations.

The M_w 8.8 27 February 2010 Maule earthquake ruptured a ~ 500-km segment of the South Chile subduction zone, which has been long identified as a seismic gap, north of the 1960 M_w 9.5 Valdivia earthquake. Following the Maule earthquake, several studies have been conducted to investigate the postseismic deformation resulting from the earthquake. Bedford et al. (2013) and Lin et al. (2013) employed elastic models to study the effect of afterslip only on the early postseismic deformation in the near field. They consistently obtained a heterogeneous afterslip distribution with maximum slip up to 2 m near the downdip end of the coseismic slip at 20–40 km depth over the first 1.5 years. Klein et al. (2016) reported 5 years continuous GPS (cGPS) measurements and combined afterslip and viscoelastic relaxation with a Burgers rheology to model the first 2 years of the 3-D GPS time series in both the near and far fields. They found that the asthenosphere has a viscosity of ~5×10^{18} Pa s and a weak subduction channel extends from depths of 55–135 km with viscosity $<10^{18}$ Pa s. Bedford et al. (2016) used a straightening method to separate the displacements generated by relocking, afterslip, and viscoelastic relaxation in 4 years of GPS time series in the near field. They found that the plate interface recovers very rapidly ($<$1 year) to its interseismic locking state. Li et al. (2017) used a viscoelastic relaxation model to explain the 6-year 3-D cumulative displacements in the far field. They argued that a spatially heterogeneous viscosity distribution is necessary to explain the long-wavelength vertical deformation pattern, which is correlated to the first-order thermal structure at depth.

Previous models that combined both afterslip and viscoelastic relaxation potentially oversimplify the inferences drawn about the viscoelastic relaxation in terms of rheological and/or viscous-structural complexity in the asthenosphere. In this work, we aim to resolve the first-order heterogeneous viscoelastic relaxation process and aim for estimating the postseismic viscosity variation not only in space but more importantly in time. To do this, we present an updated model based on Li et al. (2017) with the addition of time windowing. Furthermore, we refine the methodology of Li et al. (2017) to more precisely estimate the viscosity values by considering the potential effects of afterslip and relocking. In particular, we explore the degree to which the continental craton—the Rio de la Plata craton of Argentina (Rapela et al., 2007; Figure 1)—may affect the postseismic deformation pattern. We explore three scenarios of viscoelastic relaxation in the asthenosphere: homogeneous viscosity structure, laterally heterogeneous viscosity structure, and a refined laterally heterogeneous viscosity structure that incorporates cratonic mantle. We propose the optimal viscoelastic relaxation scenario from these three scenarios that best fit all the cumulative postseismic surface displacements recorded by cGPS stations. Comparing the results in variable cumulative time windows, we infer the evolution of the optimal viscosity structure in time. Finally, we present the implications for the mantle rheology in southern South America.

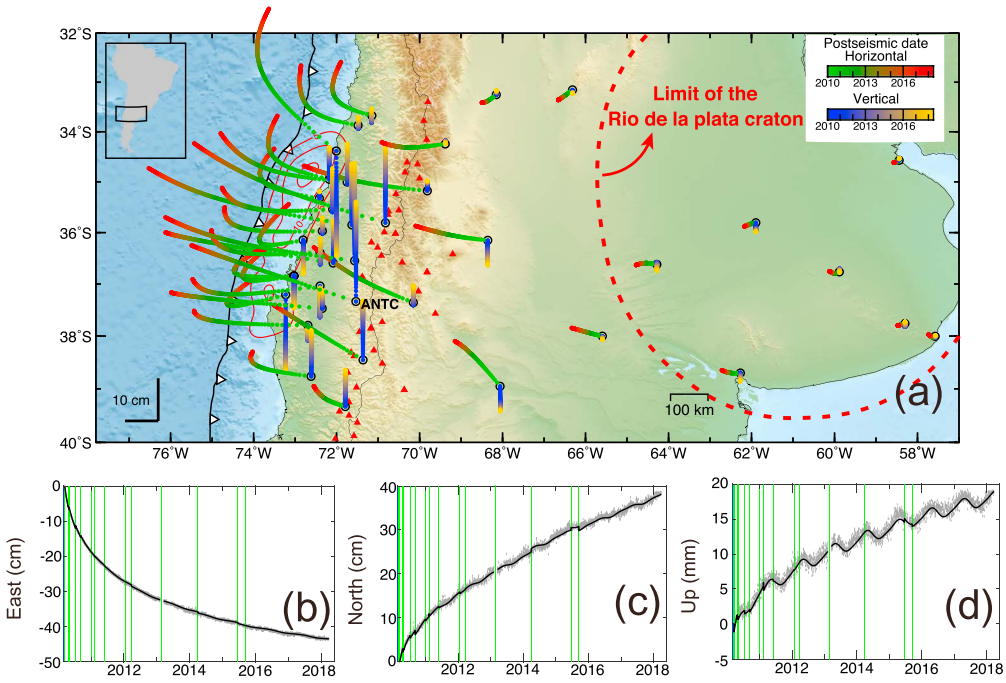

Figure 1. (a) The temporal evolution of cumulative 3-D postseismic surface displacements of 2010 Maule earthquake based on analytical fits (see text) to the GPS time series. The study area (inset) is located in South America. The red contours are the coseismic slip distribution from Moreno et al. (2012) in meters. The red triangles indicate active volcanoes. The red dashed line shows the inferred limit of the Río de la Plata craton modified from Rapela et al. (2007). (b)–(d) Examples of analytical fitting of 3-D postseismic GPS time series recorded at station ANTC (location shown in Figure 1a). Gray dots are the original daily observations. The black curves are the analytical fit. Green vertical lines denote the time of the jumps. GPS = Global Positioning System.

2. GPS Observations

We use cGPS time series processed in the IGS08 reference frame (Rebischung et al., 2012) to constrain our viscoelastic simulations. We obtained daily solutions from the Nevada Geodetic Laboratory (Nevada Bureau of Mines and Geology, University of Nevada, United States, http://geodesy.unr.edu/index.php, last accessed on 13 April 2018). We used 55 stations with observations spanning the Andes and southern Argentina and at least 3–4 years of the Maule postseismic period (Figure 1). The raw data, from which these position time series were generated (e.g., Figures 1b–1d), were mainly provided through the National Science Foundation-funded Central Andes GPS Project (Bevis et al., 2000; Kendrick et al., 1999) and the postseismic deployment organized by Chilean, École normale supérieure (ENS), Deutsches GeoForschungsZentrum (GFZ-Potsdam), Institut de Physique du Globe de Paris (IPGP), and many other groups (e.g., Bedford et al., 2016; Klein et al., 2016). The names, locations, and the access of the used stations are listed in Table S1. We modeled the trajectory of the individual GPS stations using the approach described in Li et al. (2017) and removed the displacement components not related to the postseismic processes (i.e., seasonal variations and discontinuities from antenna offsets or the coseismic displacements of small earthquakes). Note that the (steady state) interseismic trend is not removed in this approach but modeled as described further below. Cumulative postseismic displacements at any given time period can thus be determined from the remaining postseismic transients of the trajectory model. Figures 1b–1d show one example of the trajectory model of the three observational components and Figure 1a shows the temporal evolution of both horizontal and vertical pathways determined from trajectory modeling at all stations.

The temporal evolutions of 3-D postseismic displacements show distinct characteristics in the 8 years of observations (Figure 2). All stations show rapid westward (seaward) motion immediately after the Maule earthquake, which then decelerate gradually in the following years (Figure 2a). Interestingly, some stations near the coast reversed their directions to east and northward motion 3–4 years after the earthquake (denoted in the ellipse in Figure 2a). Such behavior indicates that relocking had resumed and

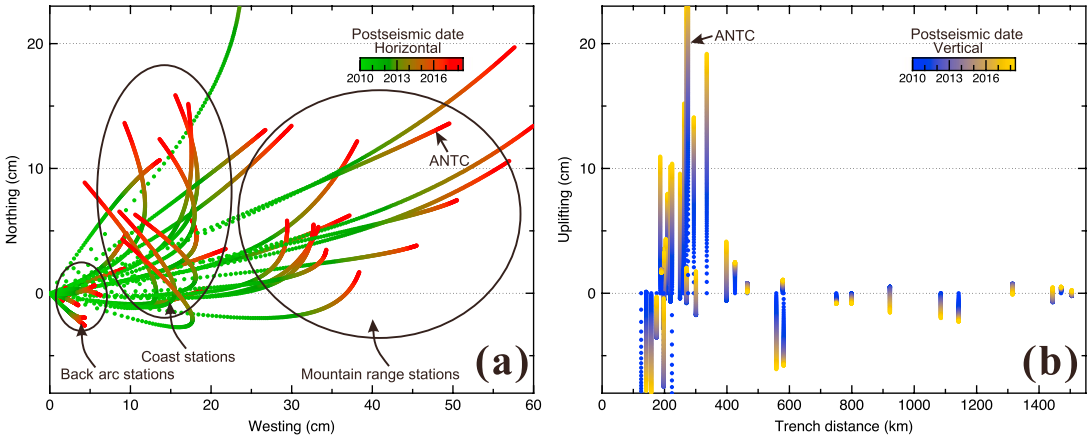

Figure 2. (a) The temporal evolution of the horizontal postseismic displacements. Stations with distinct characteristics of horizontal displacements are denoted as three groups by ellipses. (b) The temporal evolution of vertical postseismic displacements with respect to the trench distance.

overwhelmed the postseismic transient (Wang et al., 2012); the northward motion indicates the obliquity of Nazca plate convergence. The reversal of horizontal displacements propagates gradually further inland toward the mountain range with time, indicating a gradual relocking of the magthrust and/or a decay of postseismic viscoelastic relaxation (Sun et al., 2018; Wang et al., 2012). The stations located in the Andean mountain range, where the active volcanic arc is located (Hildreth & Moorbath, 1988; Figure 1a), show the largest horizontal displacements (30–60 cm cumulative displacements over 8 years), while the stations in back-arc region, where the ancient Rio de la Plata Craton is inferred (Figure 1a), show smaller but resolvable horizontal displacements (~5-cm cumulative displacements over 8 years; Figure 2a). In the vertical displacement direction, the stations show continuous subsidence near the coast (~5 cm cumulative displacements over 8 years at 100- to 200-km trench distance), significant uplift in the mountain range (~10-cm cumulative displacements over 8 years at ~200- to 500-km trench distance), and gentle subsidence in the region east of the volcanic arc (a few centimeters cumulative displacements over 8 years at 500- to 1,200-km trench distance), forming a very long-wavelength lithospheric flexure pattern (Figure 2b). Some stations near the coast also switched vertical displacement sense 3–4 years after the earthquake, from uplifting to subsiding.

3. Finite Element Modeling

3.1. Model Setup

We develop a continental-scale three-dimensional finite element model that includes elastic lithospheric (crust and upper mantle) and viscoelastic mantle asthenosphere. Our modeling approach focuses on deducing the effective viscosity heterogeneities beneath the network of GPS stations as constrained by the cumulative surface displacements. Accordingly, we assign a linear Maxwell rheology to the viscoelastic body. All numerical simulations in this study are solved with the open source finite element software PyLith (Aagaard et al., 2013). The 3-D geometry of our model incorporates the geometry of the subduction slab and the continental Moho (Figure S3a; Contreras-Reyes & Osses, 2010; Hayes et al., 2012; Tassara & Echaurren, 2012), following our previous studies of the south Central Chile area (e.g., Moreno et al., 2012). The material properties used in the modeling and their corresponding references are described in Table S2.

The model domain extends 4,000 km in the E-W direction, 2,000 km in the N-S direction, and 400 km in the vertical direction (Figure S3a). The east and west boundaries and the base of the model domain are held fixed, and the north and south boundaries and the top of the model domain have no constraints (free to move). We tested these boundary conditions and found no biasing influence on the model results. We use controlled meshing to gradually change the size of the elements in the study area (Figure S3b). To better resolve the fault slip and variation of material properties close to the oceanic slab, and to avoid distorted elements close to the trench, finer element discretization sizes are used on the continental surface (approximately 5 km), close to the oceanic slab (approximately 10 km), and close to the trench (approximately

1 km). A coarser element discretization size is assigned to the deep parts of both mantle domains (>50 km) to save computational cost. The final mesh is composed of about 1.5 million four-node tetrahedral elements in total.

We incorporate the coseismic slip distribution from Moreno et al. (2012). We find that the coseismic surface displacements predicted by this model agree with GPS observations exceedingly well in the near and far fields of the rupture (Figure S4), indicating that our model geometry, mesh, elastic material properties, and boundary conditions are appropriately defined. We then drive the postseismic simulations for an 8-year observation period using this coseismic rupture. We assume that all evidence of viscoelastic relaxation originates from the M_w 8.8 coseismic rupture, as opposed to viscoelastic relaxation induced by afterslips, aftershocks, or relocking of the megathrust.

3.2. Modeling of Relocking and Afterslip

Since this study is focused on investigating the viscoelastic relaxation of the viscosity structure which impacts mainly on the far-field postseismic deformation (e.g., Freed et al., 2007; Freed et al., 2012), we do not include the near-field stations <~300-km trench distance (i.e., the forearc area) in the analysis. The distribution of the stations selected and rejected for the analysis is shown in Figure S1. In order to more precisely estimate the mantle viscosity values, we further model and remove the first-order effects of relocking and afterslip on surface displacements at the retained far-field stations. We simulate the geodetic signature of megathrust relocking results by forward modeling of the interseismic locking distribution from Moreno et al. (2011; Figure 3a). We assume that that this model adequately describes the steady interseismic motion in all time series. Displacements due to afterslip are approximated by forward modeling of the afterslip distribution from Bedford et al. (2016; Figure 3b) and assuming a power law decay (Figure S2) following the strategies of Bedford et al. (2016) and Klein et al. (2016).

The results (Figure 3) show that these two processes counteract each other, to some extent, in terms of horizontal displacements, and both produce negligible vertical displacements in the Andes mountain area. In the area east of the mountain range, no detectable displacements are predicted from these models, indicating that plate interface processes are likely to produce short-wavelength deformation patterns, as suggested by previous studies (e.g., Pollitz et al., 1998). Consequently, viscoelastic relaxation is needed to explain the observed long-wavelength deformation pattern in the far field. As mentioned previously for simplicity, we ignore the potential scenario where viscoelastic relaxation may be influenced by relocking and afterslip.

3.3. Signatures of Cratonic Mantle on Viscoelastic Relaxation in the Far Field

Numerical modeling of near-field earthquake deformation usually involves artificial extensions of lateral model boundaries with simplification of Earth structure to a homogeneous medium in order to minimize potential boundary effects (e.g., Li et al., 2014). This simplification might be problematic when modeling the postseismic viscoelastic relaxation deformation of great earthquakes and may inappropriately ignore long-wavelength displacements that are informative of lateral heterogeneities in Earth structure. Following the 2010 Maule earthquake, detectable postseismic displacements are recorded >1,400 km from the trench in the region of the Rio de la Plata craton (Figure 1a). The effective elastic thickness of such ancient continental lithosphere is estimated >60 km according to previous geophysical studies (e.g., Pérez-Gussinyé et al., 2008), which might have an important impact on the postseismic deformation.

To examine and interrogate the potential influences of the rheological heterogeneity of a craton on the postseismic relaxation, we design a suite of synthetic models with and without the presence of cratonic mantle. The craton is assumed to be purely elastic (i.e., identical to the viscosity being infinitely large). Its west boundary is simplified as a viscosity contrast in the E-W direction, and its east boundary is set as the east border of the model. We vary the location of the western boundary of the craton (i.e., trench distance of 500, 700, and 900 km) and compare the predicted surface displacements of craton models and the laterally homogeneous model to the far-field GPS data (near the dashed line in Figure 3a).

The results (Figures 4a and 4c) show that models with and without the synthetic cratonic mantle predict a similar horizontal displacement pattern, but the models that include a cratonic mantle predict lower displacement magnitudes in the vicinity of the cratonic body. Such predictions of craton models are broadly consistent with the displacement gradient recorded by the far-field GPS stations following the Maule earthquake (Figure 4a). This indicates that the influences of cratonic mantle are apparent in postseismic GPS time series in

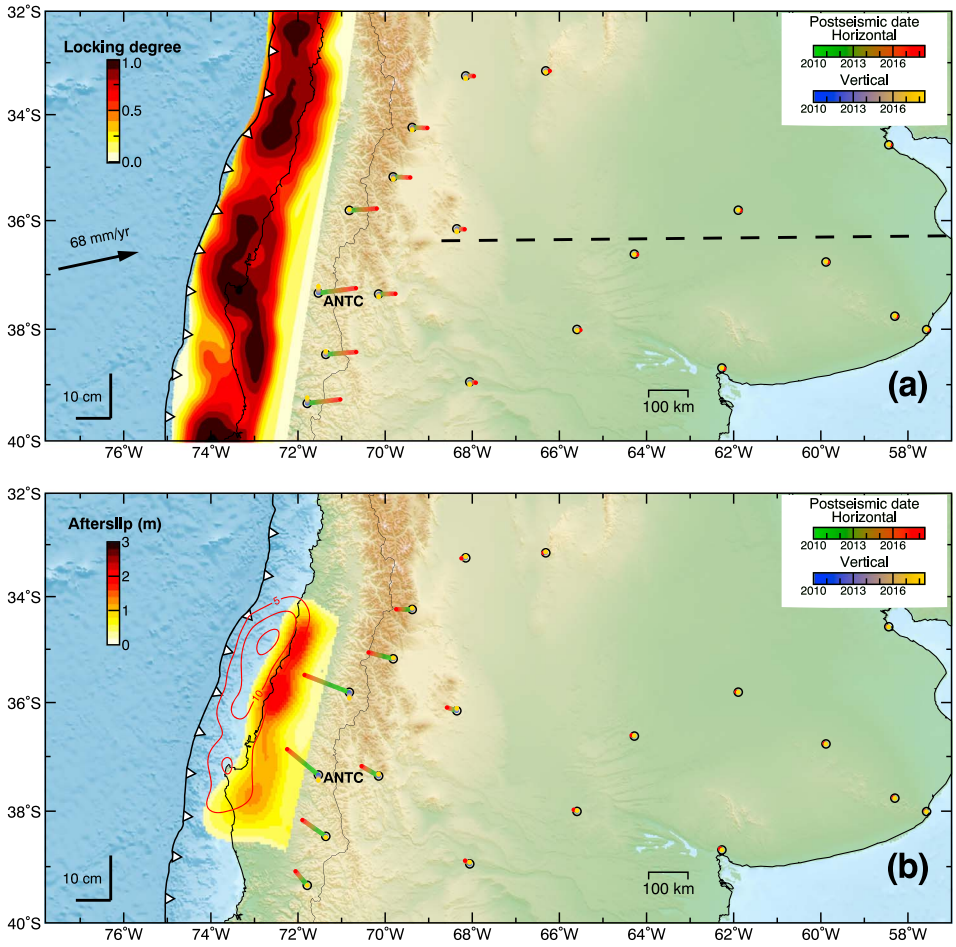

Figure 3. (a) Temporal evolution of predicted surface displacements from the interseismic locking model (Moreno et al., 2011). (b) Temporal evolution of predicted surface displacements from the afterslip model (Bedford et al., 2016). The red contours are coseismic slip distribution from Moreno et al. (2012) in meters. The legends for predicted displacements are the same as those for Figure 1a.

Argentina. The vertical displacement is decreased locally with the presence of cratonic mantle, showing a subsidence zone located around 100 km closer to the trench than the specified viscosity boundary (Figures 4b and 4d). As expected, the presence of a cratonic mantle increasingly impacts predicted displacements as the transition to the craton is placed closer to the source region of the Maule earthquake. This indicates that gradients in the displacement field may be diagnostic of the location of the edge of the craton. Considering both the horizontal and vertical deformation pattern, especially the subsidence signal around 600 km, observed by GPS sites (Figure 2b), we propose that the effective boundary of cratonic mantle is roughly 700 km from the trench (consistent with Li et al., 2017) and propose a refinement model in section 3.4.

3.4. Determining Viscosity Structures in Cumulative Time Windows

Here we describe our modeling approach to interrogate the spatiotemporal variations in asthenosphere viscosity in the study area. To ensure that the change of the cumulative static displacement can be interpreted as reflecting viscosity variation within the modeling sensitivity, we discretize the cumulative displacement time series into expanding 1-year intervals (i.e., the explored time windows are 0–1, 0–2, 0–3, 0–4, 0–5, 0–6, 0–7, and 0–8 years). Within each window, the cumulative postseismic displacements of each GPS station are determined by the time series analysis described in section 2.

For viscoelastic models, we consider three scenarios (Figure 5) of viscoelastic structure in the asthenosphere: scenario A, equivalent oceanic and continental mantle rheologies (i.e., the homogeneous model); scenario B, laterally heterogeneous model following the strategy of Li et al. (2017) with the viscoelastic mantle properties

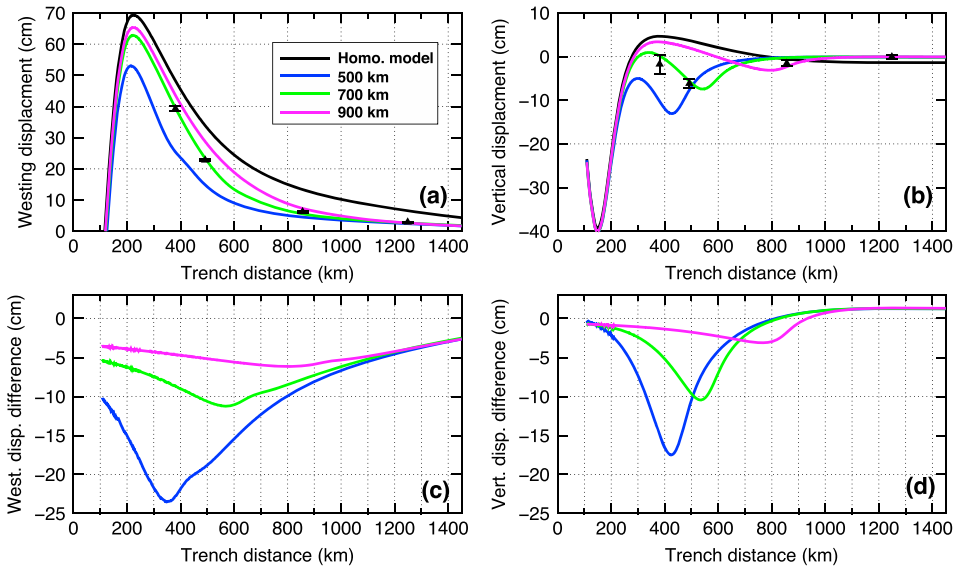

Figure 4. Illustrations showing the influence of a synthetic cratonic mantle on surface deformation. The postseismic displacements are simulated by imposing the coseismic slip of Moreno et al. (2012) and relaxing the viscoelastic mantle for 8 years. The mantle viscosity of the homogeneous model is assumed as 5×10^{18} Pa s. The numbers of 500, 700, and 900 km mean the trench distances of the west boundary of the synthetic craton. (a and b) The modeling displacements from different end-member models in horizontal and vertical directions, respectively. The far-field GPS data are plotted to benchmark these models. The predicted displacements of relocking and afterslip are removed from the GPS data, and the locations of these stations are near the dashed line in Figure 3a. (c and d) Displacement differences between craton models and homogeneous models in the horizontal and vertical directions, respectively. GPS = Global Positioning System.

constrained by the time dependence observed at the GPS stations above it (Figure S5); and scenario C, a laterally heterogeneous model assigned elastic behavior at distances greater than 700 km from the trench to approximate the effects of the Rio de la Plata craton based on the simulation described in section 3.3. We do not attempt to further refine the distance to the craton, the 3-D shape of the craton, or the viscosity of the craton given the relatively sparse station distribution in the far field.

For each of the model iterations, we use different strategies to determine the optimal viscosity. For the homogeneous model (scenario A, Figure 5a), we iterate through a range of viscosities (i.e., 10^{17} to 10^{22} Pa s, lower or higher viscosity is found unnecessary to explain the displacements) and choose the optimal viscosity that can best explain all the GPS displacements. For the two heterogeneous viscosity structures (i.e., scenarios B and C), we first find the optimal viscosity that best fits each GPS station, on a station-by-station basis and within the expanding time intervals described above, by selecting the viscosity of the homogeneous viscoelastic model that minimizes the weighted root-mean-square (WRMS) misfit of the station (e.g., Figure 6a, following the approach of Li et al., 2017). With the optimal viscosity values determined at all stations, we then construct the heterogeneous viscoelastic mantle structures for scenarios B and C (Figures 5b and 5c). Finally, we justify the heterogeneous viscosity structures by forward models and compare their performances in terms of fitting the cumulative horizontal and vertical displacements of all the used stations.

4. Results

We explore the viscoelastic relaxations of forward models (i.e., scenarios A–C) in response to the Maule earthquake in the variable time windows. The performances of the three models are summarized in Figure 6b in terms of the summed WRMS misfit of all the 3-D cumulative GPS displacements and model predictions. The homogeneous viscosity needed to fit the cumulative displacements increases with the length of the cumulative time window (denoted above the green curve in Figure 6b), indicating asthenosphere viscosity increases with time after the earthquake. Increasing the lateral complexity of our models leads to increasingly better fits to the GPS observations (i.e., scenario C performs better than scenario B, and scenario B performs better than scenario A). Such performances are found consistent in all the time

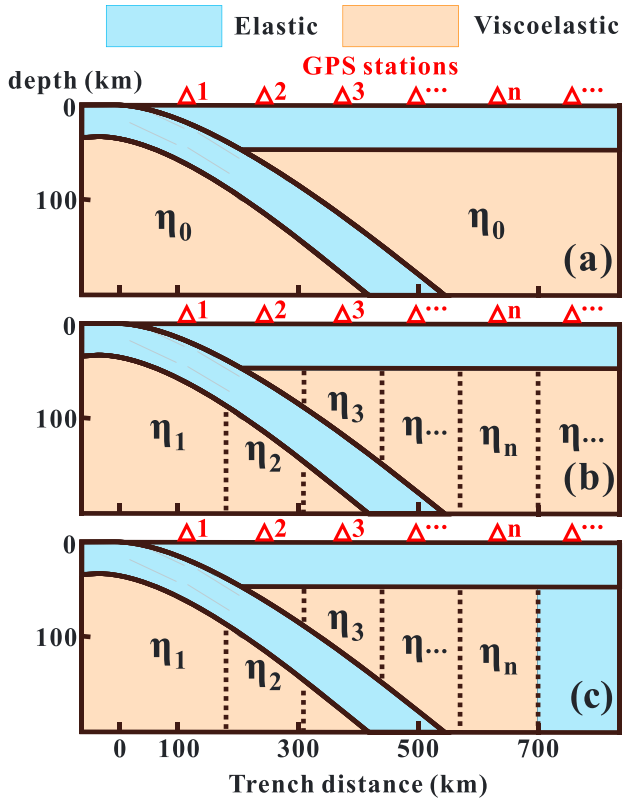

Figure 5. Illustrations of three different scenarios used for modeling the postseismic viscoelastic structure. (a) The asthenosphere is viscoelastically homogeneous. (b) The asthenosphere is divided by projecting the Global Positioning System stations vertically down, following the strategy of Li et al. (2017). (c) The same as (b) but the field >700 km trench distance is assigned with elastic material. The variables denoted within the dashed blocks are the values of viscosity to be constrained in the viscoelastic modeling.

windows, indicating the first-order importance of lateral viscosity variation in the asthenosphere at trench distances between 300 and 700 km and the presence of a stationary cratonic mantle at trench distance >700 km. The fits of scenarios A–C to the 3-D GPS observations for two time windows (i.e., 0–1 and 0–8 years) are shown in Figure 7, and other time windows are shown in Figures S6–S12.

The optimal heterogeneous viscosity structure is therefore proposed in this study as scenario C. Figure 8 shows the temporal evolution of the optimal viscosity distribution in the intermediate-to-far-field range (trench distance of 200–700 km). In order to better illustrate the viscosity variation away from the rupture zone in time, we take swath profiles along the viscosity maps (the dashed lines Figure 8a), normal to the center of the coseismic rupture zone. Figure 10d shows averaged values of these profiles for the eight investigated cumulative time spans. The results clearly show that the viscosities needed to fit the cumulative displacements increase with increasing time after the earthquake. Moreover, the rate of viscosity change is fastest in the regions closest to the trench and at the time immediately after the earthquake, and this rate progressively decreases with increasing distance from the trench and elapsed time after the earthquake. This result likely illustrates the stress/strain-rate dependence of viscous flow. The far field (>700-km trench distance) behaves almost elastically (not plotted in Figure 8), and no significant temporal variation of the viscosity is inferred in our study probably due to the presence of the strong cratonic mantle in Argentina in combination with distal small stress changes.

Overall, the heterogeneous viscosity distribution and its variations in different cumulative time windows have three main characteristics: (1) viscosities increase at most a factor of 6 of magnitude with increasing distance from the trench immediately after the earthquake (i.e., from 2×10^{18} Pa s in the area of <300-km trench distance to 10^{19} Pa s in the area of <700-km trench distance) and become more

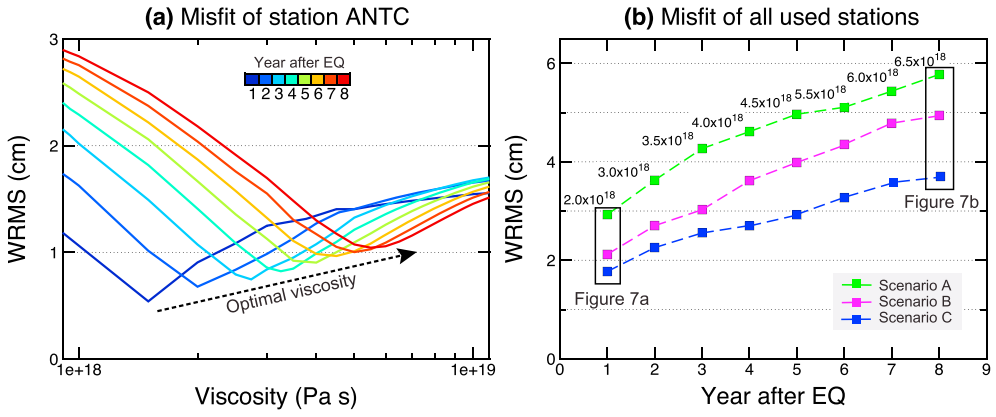

Figure 6. (a) An example (i.e., station ANTC; for the location see Figure 1) of determining the optimal viscosity by selecting the best fit of the cumulative horizontal GPS displacements in terms of lowest of WRMS. (b) The performance of scenarios A–C in fitting all the cumulative horizontal and vertical GPS observations in different elapsed time windows. The optimal homogeneous viscosity values (in pascal-second) of scenario A in different elapsed time windows are additionally denoted as black text. GPS = Global Positioning System; WRMS = weighted root mean square; EQ = earthquake.

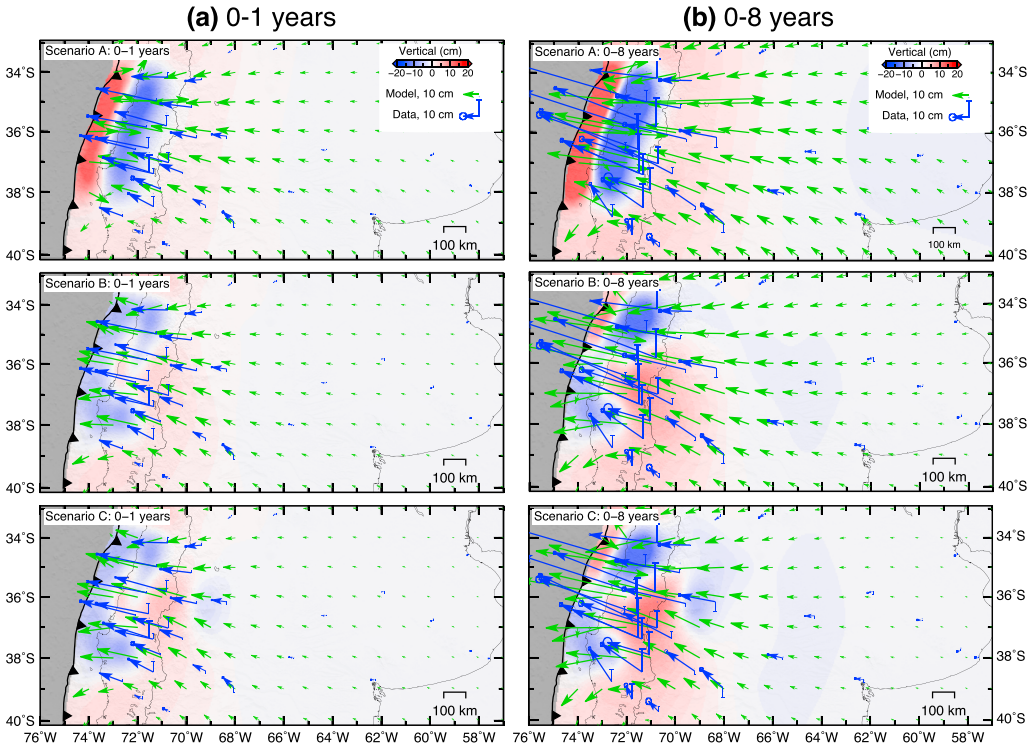

Figure 7. The fits of cumulative displacements of viscoelastic relaxation in the time windows of 0–1 years (a) and 0–8 years (b) using models of scenarios A–C. Modeled relocking and afterslip displacements of the Maule earthquake have been removed from the Global Positioning System data.

laterally homogeneous with longer time after the earthquake; (2) viscosities increase rapidly immediately after the earthquake and the rate of change gradually slows down over the 8 years observation time, and the rate of viscosity change decreases with increasing distance in the area of trench distance between 300 and 700 km; (3) viscosity at trench distance >700 km is as high as almost being elastic and invariant with time, at least within the resolution capability of the GPS observation.

5. Discussion

A rapid international effort was made to monitor the Earth's surface deformation after the 2010 Maule earthquake with a dense array of cGPS stations installed by Chilean, German, French, American, and Argentinean groups (e.g., Schurr et al., 2009). The onshore side of the rupture zone is very well covered by cGPS stations from the coastline, at only some 100 km from the trench, up to a distance of about 1,500 km from the trench (Figure 1a). This network provides a unique opportunity to monitor very long wavelength postseismic deformation of a great subduction earthquake as well as its temporal evolution. Spatially, the entire continental plate moves horizontally toward the rupture zone with displacement gradient decreasing significantly in the hinterland area (Figure 1a). Moreover, the South America plate deforms vertically with subsidence near the coast, peak uplift in the Andean mountain range, and subsidence in the hinterland forming a flexure pattern (Figure 2b). Such a 3-D deformation pattern is similar to that of the 2011 Tohoku-oki earthquake (see data shown in Freed et al., 2017), perhaps representing a typical and first-order deformation pattern following a great subduction zone earthquake. Temporally, and perhaps more interestingly, the evolution of the 3-D displacements show many intriguing characteristics. For instance, the coast area reversed its seaward motion to landward motion, aligning with the oblique convergence direction of the Nazca plate 3–4 years after the earthquake (Figure 2a). This realignment of GPS vectors is currently propagating further inland. Eventually, all the GPS vectors on the continental plate will return to the interseismic state that preceded the 2010 Maule earthquake (Moreno et al., 2010), completing a full postseismic deformation cycle (Wang et al., 2012). When and how the system arrives at this state requires longer observation and further quantitative investigations.

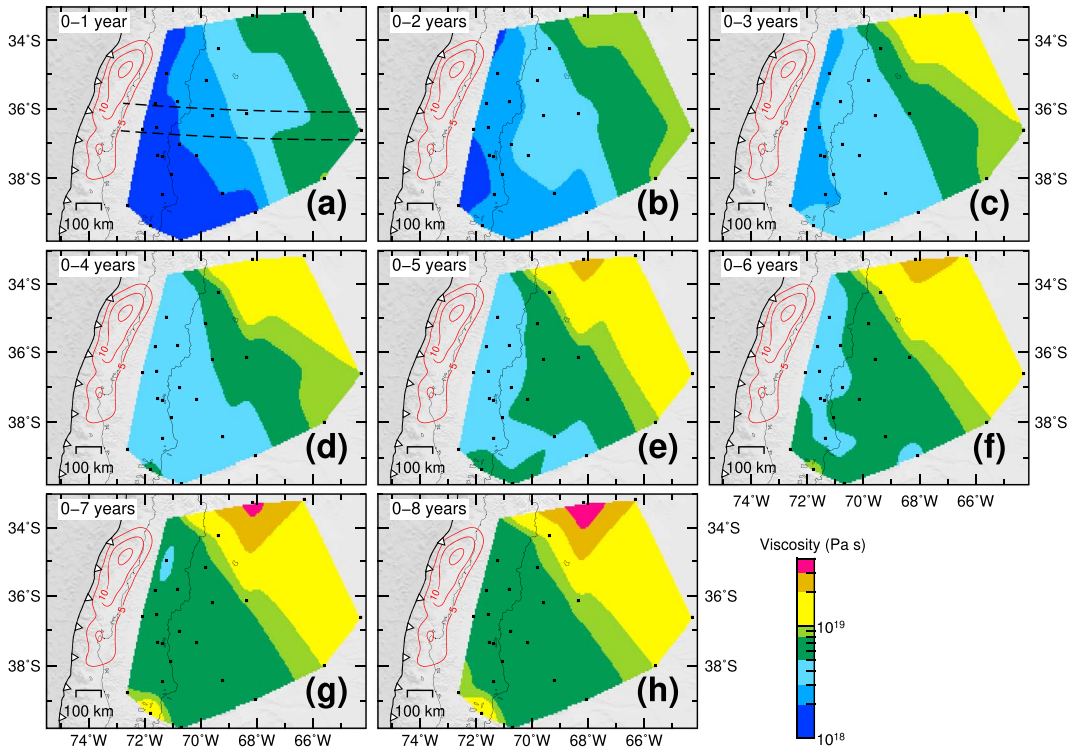

Figure 8. The optimal viscosity distribution of the intermediate-to-far-field range (trench distance of 200–700 km) in (a–h) different cumulative time windows since the mainshock. The far field (>700-km trench distance) behaves almost elastically, and the viscosity distribution is hence not plotted here. The black squares are the continuous Global Positioning System stations. The red contours are coseismic slip distribution from Moreno et al. (2012) in meters.

In this study, we focused on resolving the temporal evolution of mantle viscosities informed by the viscoelastic relaxation in the intermediate-to-far to far-field range (>300 km trench distance), and we neglected the near-field data (<300 km trench distance) that may be affected by multiple processes (i.e., afterslip, relocking, poroelastic rebound, and viscoelastic relaxation). Some recent studies consider a combination of viscoelastic relaxation and afterslip to explain the postseismic deformation but assign a simplified viscous structure in asthenosphere, especially in the lateral direction, to determine the viscoelastic relaxation contribution (e.g., Bedford et al., 2016; Freed et al., 2017). Such simplifications sometimes underestimate the importance of viscoelastic relaxation, leading to incorrect determinations of afterslip (e.g., Sun & Wang, 2015). Consequently, a study such as this one aimed toward resolving the viscoelastic relaxation alone might contribute to greater confidence separating these two processes. With better data precision and longer data accumulation, the vertical observations might be significantly important in discriminating between afterslip and viscoelastic relaxation.

In this study, we avoid unnecessary assumptions (e.g., viscosity structure and time evolution of viscosity) by starting from the simplest homogeneous models and then increase the necessary model complexities. In doing so, we progressively gain insights into the first-order mechanisms of viscoelastic relaxation, as evidenced by the improvement of model misfit (Figure 6b). Our results suggest that the spatial distribution of postseismic viscosity is laterally heterogeneous across strike of the subduction zone. The heterogeneous viscosity distribution exhibits a first-order lateral segmentation with relatively low viscosity (~ 10^{18} Pa s) below the volcanic area and a highly viscous (> 10^{22} Pa s) cratonic mantle in the far field (Figure 10a). As previously proposed by Li et al. (2017), this distribution might indicate the first-order influences of decreasing temperatures on viscosity (Figures 10b and 10d); that is, the high geothermal gradient beneath the Andean mountain range and the low geothermal gradient beneath the cratonic mantle in Argentina correspond to relatively low and high viscosity, respectively. We note that the viscosity distribution may also relate to the fluid content, especially in volcanic arcs (e.g., Masuti et al., 2016), and the

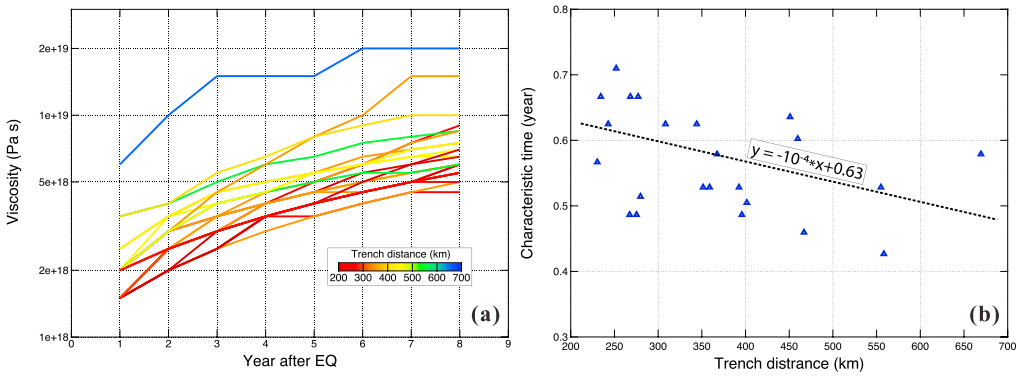

Figure 9. Spatial dependence (a) and characteristic time (b) of the viscosity evolution in the intermediate-to-far-field range (trench distance of 200–700 km). The characteristic time is estimated from the optimal exponential function that describes the time evolution of the viscosity. EQ = earthquake.

data fitting of scenario C may be further improved with better optimized 3-D shape and viscosity of the cratonic mantle. Nevertheless, the viscosity (2–6 × 10^{18} Pa s, Figure 10d) estimated in the mantle wedge in this study is, surprisingly, of the same order of magnitude as the viscosity of the asthenosphere (~5 × 10^{18} Pa s) estimated by Klein et al. (2016) for the 2010 M_w 8.8 Maule earthquake, as the viscosity of asthenosphere (3 × 10^{18} Pa s) estimated by Wiseman et al. (2015) for the 2004 M_w 9.2 Sumatra-Andaman earthquake, and as the viscosity of asthenosphere (2–4 × 10^{18} Pa s) estimated by Freed et al. (2017) for the 2010 M_w 9.1 Tohuku-oki, Japan, earthquake. This viscosity (i.e., a few 10^{18} Pa s) may represent the average value of mantle wedge globally, which is an order of magnitude lower than the global average value of the asthenosphere (Wang et al., 2012). This study further suggests that the viscosity of the cratonic mantle remains almost constant in the 8-year postseismic period, indicating the stationary presence of the ancient craton in the far field (Figure 10a). Interestingly, the performance of scenario C is increasingly better than that of scenario B with passing time (Figure 6b), indicating that the long-term geological feature is surpassing the short-term earthquake effects on the postseismic transient. We therefore anticipate that the lateral viscosity heterogeneities may also impact on the (subtle) interseismic deformation in Maule area as well as other subduction zones, calling for future studies.

This study shows that the viscosity structure recovers gradually after the megathrust earthquake (Figures 8, 9a, and 10d). Therefore, the stationary viscosity distribution constrained by static displacement field in previous postseismic studies (e.g., Freed et al., 2017; Li et al., 2017) may only represent a snapshot of the varying viscosity in the time span of available observations. The finding of viscosity variation in time confirms that transient rheology (e.g., Burgers rheology) is necessary to fit the nonlinear rate changes of the displacement time series and is consistent with geodetic and numerical modeling results obtained with other methodologies (e.g., Barbot, 2018; Qiu et al., 2018; Masuti et al., 2016; Sobolev & Muldashev, 2017). Interestingly, the area close to the rupture zone recovers its viscosity faster than the area away from the rupture zone (Figures 9a and 10d), indicating a stress/strain rate dependence component of the viscosity (Figure 10c), in agreement with laboratory experiments. In order to further quantitatively test whether the viscosity recovery is consistent with power law rheology, we estimate the characteristic time (T_c, in year) of the viscosity evolution at the retained stations in the intermediate-to-far-field range (trench distance of 200–700 km; Figure 9b). T_c is estimated by the formula $\eta_t = \eta_0 e^{-(t/T_c)}$, where t is the Maule earthquake elapsed time in year and η is the estimated viscosity in pascal-second. We find that T_c decays generally with the distance to the trench, consistent with the power law rheology. Accordingly, we propose that the spatial viscosity distribution is mainly dependent on the geothermal structure at depth and the temporal viscosity evolution is mainly dependent on the earthquake-introduced stress variation (Figure 10). However, the relative contribution of these two components needs further quantitative investigations.

The layering of Earth structure is not considered in our models. Adding depth-dependent layers (e.g., Freed et al., 2017) might improve the GPS displacements fitting and confirm the viscosity being dependent on

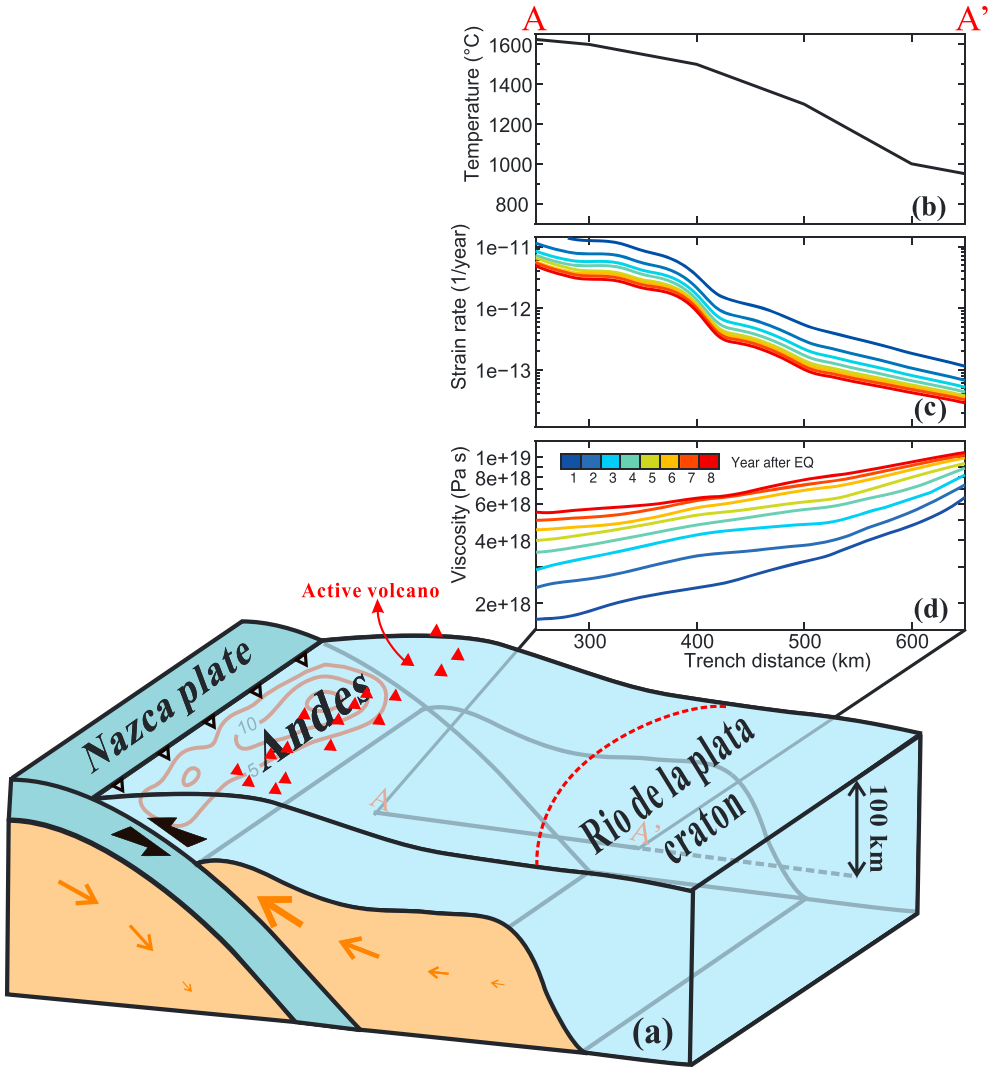

Figure 10. (a) Schematic illustration of the viscoelastic relaxation scenario inferred from 7 years postseismic deformation of the 2010 Maule Chile earthquake. (b–d) The spatiotemporal correlations of temperature and strain rate with viscosity. (a) The temperature variation (at 100 km depth) with the trench distance from (Springer, 1999). (b) The calculated second invariant strain rate (at 100 km depth) of the swath profile for different cumulative time windows. (c) The averaged viscosity of the swath profile for different cumulative time windows. The location of the swath profile is plotted in Figure 8a as the dashed lines.

depth-varying temperature, pressure, and water content (Hirth & Kohlstedt, 1996). However, the degrees of freedom and consequently the number of possible models increase exponentially with the number of free layers as well as the number of combinations of their thicknesses. Resolving a modest number of additional free layers would increase the computational cost beyond our current resources, and even then, great ambiguity might arise from the layer thicknesses (e.g., (Hines & Hetland, 2013; Johnson et al., 2007; Riva & Govers, 2009). Essentially, there is also a trade-off between the chosen depths of the layer boundaries and the modeling-constrained viscosities in the layers (e.g., Freed et al., 2017; Hu et al., 2016). A caveat of this study is that the viscosity distribution is constrained in cumulative time windows and therefore a direct quantitative comparison of the viscosity variation in different time windows is not fully accurate because of the neglect of the effects of the stress variation caused by the viscosity evolution. A self-consistent model with continuous spatiotemporal viscosity variation would be more realistic and might shed light on fully explaining the trajectory of 3-D GPS time series, which remains a challenge for postseismic models.

6. Conclusion

We exploit the 8-years time series of cumulative GPS displacements after the 2010 M_w 8.8 Maule Chile earthquake to constrain the deep viscosity structure and its temporal evolution. We remove the first-order potential influences of afterslip and relocking on our estimations of mantle viscosities >300-km trench distance. Comparing the fitting of the 3-D finite element viscoelastic models to the GPS observations, we propose a spatially and temporally varying viscosity in the asthenosphere. The viscosity scenario shows significant lateral increment in space with the viscosity of 10^{18} Pa s in the area of ~300-km trench distance, 10^{19} Pa s in the area of ~700-km trench distance, and an almost elastic cratonic mantle in the area of >700-km trench distance. During the 8 years after the earthquake, the viscosity recovers gradually by at least 1 order of magnitude (i.e., from ~10^{18} to ~10^{19} Pa s) in the area of from 300- to 700-km trench distance and may keep constant in the area of >700 km trench distance due to the presence of the cratonic mantle in Argentina. Such spatiotemporal variation of viscosity implies both temperature and stress/strain rate dependence of the viscosity in terms of transient rheology and needs to be considered in modeling the earthquake cycle deformation.

Acknowledgments

Shaoyang Li was supported by a fellowship granted by the Helmholtz graduate research school GeoSim. Marcos Moreno acknowledges support from the Chilean National Fund for Development of Science and Technology (FONDECYT) grants 1181479, German Science Foundation (DFG) grants MO 2310/3-1, the Millennium Nucleus The Seismic Cycle Along Subduction Zones funded by the Millennium Scientific Initiative (ICM) of the Chilean Government grant NC160025, and Research Center for Integrated Disaster Risk Management (CIGIDEN), CONICYT/FONDAP 15110017. Jonathan Bedford is supported by the German Science Foundation (DFG) grant MO-2310/3-1. The postseismic daily time series are from Nevada Geodetic Laboratory (http://geodesy.unr.edu/index.php), and the raw data of the CAP project can be accessed through UNAVCO (doi:10.7283/T5348HPB). We acknowledge Michael Bevis, Benjamin Brooks, Universidad de Concepcion, Universidad de Chile, Instituto Geografico Nacional de Argentina, IPGP, ENS, GFZ-Potsdam, UNAVCO, and many other groups or agencies for sharing their data to the Nevada Geodetic Laboratory through the open data policy. Postseismic modeling results for this paper are available by contacting Shaoyang Li at shaoyang-li@uiowa.edu. The authors would like to thank the developers of the open source PyLith software for their ongoing dedication to the software development and generous technical support. Discussions with Oliver Heidbach, Roland Burgmann, and Kelin Wang on an earlier version of this paper are gratefully acknowledged, and the discussion with Iskander Muldashev was helpful. We are grateful for Corné Kreemer's assistance on data citation. We thank Maureen Long, Jeffrey T. Freymueller, and two anonymous reviewers for constructive comments that greatly improved this manuscript. Most of the figures in this paper were created with GMT software (Wessel & Smith, 1998).

References

Aagaard, B. T., Knepley, M. G., & Williams, C. A. (2013). A domain decomposition approach to implementing fault slip in finite-element models of quasi-static and dynamic crustal deformation. *Journal of Geophysical Research: Solid Earth*, *118*, 3059–3079. https://doi.org/10.1002/jgrb.50217

Barbot, S. (2018). Asthenosphere flow modulated by megathrust earthquake cycles. *Geophysical Research Letters*, *45*, 6018–6031. https://doi.org/10.1029/2018GL078197

Bedford, J., Moreno, M., Baez, J. C., Lange, D., Tilmann, F., Rosenau, M., et al. (2013). A high-resolution, time-variable afterslip model for the 2010 Maule M_w = 8.8, Chile megathrust earthquake. *Earth and Planetary Science Letters*, *383*, 26–36. https://doi.org/10.1016/j.epsl.2013.09.020

Bedford, J., Moreno, M., Li, S., Oncken, O., Baez, J. C., Bevis, M., et al. (2016). Separating rapid relocking, afterslip, and viscoelastic relaxation: An application of the postseismic straightening method to the Maule 2010 cGPS. *Journal of Geophysical Research: Solid Earth*, *121*, 7618–7638. https://doi.org/10.1002/2016JB013093

Bevis, M., Kendrick, E. C., Smalley, R., Herring, T., Godoy, J., & Galban, F. (2000). Crustal motion north and south of the Arica deflection: Comparing recent geodetic results from the Central Andes. *Geochemistry, Geophysics, Geosystems*, *1*(12). https://doi.org/10.1029/1999GC000011

Burgmann, R., & Dresen, G. (2008). Rheology of the lower crust and upper mantle: Evidence from rock mechanics, geodesy and field observations. *Annual Review of Earth and Planetary Sciences*, *36*(1), 531–567. https://doi.org/10.1146/annurev.earth.36.031207.124326

Contreras-Reyes, E., & Osses, A. (2010). Lithospheric flexure modelling seaward of the Chile trench: Implications for oceanic plate weakening in the trench outer rise region. *Geophysical Journal International*, *182*(1), 97–112.

Freed, A., & Burgmann, R. (2004). Evidence of power-law flow in the Mojave desert mantle. *Nature*, *430*(6999), 548–551. https://doi.org/10.1038/nature02784

Freed, A., Burgmann, R., & Herring, T. (2007). Far-reaching transient motions after Mojave earthquakes require broad mantle flow beneath a strong crust. *Geophysical Research Letters*, *34*, L19302. https://doi.org/10.1029/2007GL030959

Freed, A., Hashima, A., Becker, T., Okaya, D., Sato, H., & Hatanaka, Y. (2017). Resolving depth-dependent subduction zone viscosity and afterslip from postseismic displacements following the 2011 Tohoku-oki, Japan earthquake. *Earth and Planetary Science Letters*, *459*, 279–290. https://doi.org/10.1016/j.epsl.2016.11.040

Freed, A., Hirth, G., & Behn, M. (2012). Using short-term postseismic displacements to infer the ambient deformation conditions of the upper mantle. *Journal of Geophysical Research*, *117*, B01409. https://doi.org/10.1029/2011JB008562

Hayes, G. P., Wald, D. J., & Johnson, R. L. (2012). Slab1.0: A three-dimensional model of global subduction zone geometries. *Journal of Geophysical Research*, *117*, B01302. https://doi.org/10.1029/2011JB008524

Hildreth, W., & Moorbath, S. (1988). Crustal contributions to arc magmatism in the Andes of Central Chile. *Contributions to Mineralogy and Petrology*, *98*(4), 455–489. https://doi.org/10.1007/BF00372365

Hines, T. T., & Hetland, E. A. (2013). Bias in estimates of lithosphere viscosity from interseismic deformation. *Geophysical Research Letters*, *40*, 4260–4265. https://doi.org/10.1002/grl.50839

Hirth, G., & Kohlstedt, D. L. (1996). Water in the oceanic upper mantle: Implications for rheology, melt extraction and the evolution of the lithosphere. *Earth and Planetary Science Letters*, *144*(1-2), 93–108. https://doi.org/10.1016/0012-821X(96)00154-9

Hu, Y., Bürgmann, R., Banerjee, P., Feng, L., Hill, E. M., Ito, T., et al. (2016). Asthenosphere rheology inferred from observations of the 2012 Indian Ocean earthquake. *Nature*, *538*(7625), 368–372. https://doi.org/10.1038/nature19787

Hussain, E., Wright, T. J., Walters, R. J., Bekaert, D. P., Lloyd, R., & Hooper, A. (2018). Constant strain accumulation rate between major earthquakes on the north Anatolian fault. *Nature Communications*, *9*(1), 1392. https://doi.org/10.1038/s41467-018-03739-2

Johnson, K. M., Hilley, G. E., & Bürgmann, R. (2007). Influence of lithosphere viscosity structure on estimates of fault slip rate in the Mojave region of the San Andreas fault system. *Journal of Geophysical Research*, *112*, B07408. https://doi.org/10.1029/2006JB004842

Kendrick, E. C., Bevis, M., Smalley, R. F., Cifuentes, O., & Galban, F. (1999). Current rates of convergence across the Central Andes: Estimates from continuous GPS observations. *Geophysical Research Letters*, *26*(5), 541–544. https://doi.org/10.1029/1999GL900040

Kirby, S. H., & Kronenberg, A. K. (1987). Rheology of the lithosphere: Selected topics. *Reviews of Geophysics*, *25*(6), 1219–1244. https://doi.org/10.1029/RG025i006p01219

Klein, E., Fleitout, L., Vigny, C., & Garaud, J. D. (2016). Afterslip and viscoelastic relaxation model inferred from the large-scale post-seismic deformation following the 2010 M_w 8.8 Maule earthquake (Chile). *Geophysical Journal International*, *205*(3), 1455–1472. https://doi.org/10.1093/gji/ggw086

Li, S., Moreno, M., Bedford, J., Rosenau, M., Heidbach, O., Melnick, D., & Oncken, O. (2017). Postseismic uplift of the Andes following the 2010 Maule earthquake: Implications for mantle rheology. *Geophysical Research Letters*, *44*, 1768–1776. https://doi.org/10.1002/2016GL071995

Li, S., Moreno, M., Rosenau, M., Melnick, D., & Oncken, O. (2014). Splay fault triggering by great subduction earthquakes inferred from finite element models. *Geophysical Research Letters*, *41*, 385–391. https://doi.org/10.1002/2013GL058598

Lin, Y.-N. N., Sladen, A., Ortega-Culaciati, F., Simons, M., Avouac, J.-P., Fielding, E. J., et al. (2013). Coseismic and postseismic slip associated with the 2010 Maule earthquake, Chile: Characterizing the Arauco Peninsula barrier effect. *Journal of Geophysical Research: Solid Earth*, *118*, 3142–3159. https://doi.org/10.1002/jgrb.50207

Malservisi, R., Schwartz, S. Y., Voss, N., Protti, M., Gonzalez, V., Dixon, T. H., et al. (2015). Multiscale postseismic behavior on a megathrust: The 2012 Nicoya earthquake, Costa Rica. *Geochemistry, Geophysics, Geosystems*, *16*, 1848–1864. https://doi.org/10.1002/2015GC005794

Masuti, S., Barbot, S. D., Karato, S. I., Feng, L., & Banerjee, P. (2016). Upper-mantle water stratification inferred from observations of the 2012 Indian Ocean earthquake. *Nature*, *538*(7625), 373–377. https://doi.org/10.1038/nature19783

Moore, J. D. P., Yu, H., Tang, C. H., Wang, T., Barbot, S., Peng, D., et al. (2017). Imaging the distribution of transient viscosity after the 2016 M_w 7.1 Kumamoto earthquake. *Science*, *356*(6334), 163–167. https://doi.org/10.1126/science.aal3422

Moreno, M., Melnick, D., Rosenau, M., Baez, J., Klotz, J., Oncken, O., et al. (2012). Toward understanding tectonic control on the M_w 8.8 2010 Maule Chile earthquake. *Earth and Planetary Science Letters*, *321–322*, 152–165.

Moreno, M., Melnick, D., Rosenau, M., Bolte, J., Klotz, J., Echtler, H., et al. (2011). Heterogeneous plate locking in the south–central Chile subduction zone: Building up the next great earthquake. *Earth and Planetary Science Letters*, *305*(3–4), 413–424. https://doi.org/10.1016/j.epsl.2011.03.025

Moreno, M., Rosenau, M., & Oncken, O. (2010). Maule earthquake slip correlates with pre-seismic locking of Andean subduction zone. *Nature*, *467*(7312), 198–202. https://doi.org/10.1038/nature09349

Nur, A., & Mavko, G. (1974). Postseismic viscoelastic rebound. *Science*, *183*(4121), 204–206. https://doi.org/10.1126/science.183.4121.204

Pérez-Gussinyé, M., Lowry, A. R., Phipps Morgan, J., & Tassara, A. (2008). Effective elastic thickness variations along the Andean margin and their relationship to subduction geometry. *Geochemistry, Geophysics, Geosystems*, *9*, Q02003. https://doi.org/10.1029/2007GC001786

Pollitz, F. (2003). Transient rheology of the uppermost mantle beneath the Mojave Desert, California. *Earth and Planetary Science Letters*, *215*, 89–104.

Pollitz, F., Wicks, C., & Thatcher, W. (2001). Mantle flow beneath a continental strike-slip fault: Postseismic deformation after the 1999 Hector Mine earthquake. *Science*, *293*(5536), 1814–1818. https://doi.org/10.1126/science.1061361

Pollitz, F. F., Bürgmann, R., & Segall, P. (1998). Joint estimation of afterslip rate and postseismic relaxation following the 1989 Loma Prieta earthquake. *Journal of Geophysical Research*, *103*(B11), 26975–26992. https://doi.org/10.1029/98JB01554

Qiu, Q., Moore, J. D., Barbot, S., Feng, L., & Hill, E. M. (2018). Transient rheology of the Sumatran mantle wedge revealed by a decade of great earthquakes. *Nature Communications*, *9*(1), 995. https://doi.org/10.1038/s41467-018-03298-6

Rapela, C. W., Pankhurst, R. J., Casquet, C., Fanning, C. M., Baldo, E. G., González-Casado, J. M., et al. (2007). The Río de la Plata craton and the assembly of SW Gondwana. *Earth-Science Reviews*, *83*(1-2), 49–82. https://doi.org/10.1016/j.earscirev.2007.03.004

Rebischung, P., Griffiths, J., Ray, J., Schmid, R., Collilieux, X., & Garayt, B. (2012). IGS08: The IGS realization of ITRF2008. *GPS Solutions*, *16*(4), 483–494. https://doi.org/10.1007/s10291-011-0248-2

Riva, R. E. M., & Govers, R. (2009). Relating viscosities from postseismic relaxation to a realistic viscosity structure for the lithosphere. *Geophysical Journal International*, *176*(2), 614–624. https://doi.org/10.1111/j.1365-246X.2008.04004.x

Schurr, B., A. Asch, F. Sodoudi, A. Manzanares, O. Ritter, J. Klotz, et al. (2009). The International Plate Boundary Observatory Chile (IPOC) in the northern Chile seismic gap, paper presented at EGU General Assembly Conference Abstracts.

Sobolev, S. V., & Muldashev, I. A. (2017). Modeling seismic cycles of great megathrust earthquakes across the scales with focus at postseismic phase. *Geochemistry, Geophysics, Geosystems*, *18*, 4387–4408. https://doi.org/10.1002/2017GC007230

Springer, M. (1999). Interpretation of heat-flow density in the Central Andes. *Tectonophysics*, *306*(3–4), 377–395. https://doi.org/10.1016/S0040-1951(99)00067-0

Sun, T., & Wang, K. (2015). Viscoelastic relaxation following subduction earthquakes and its effects on afterslip determination. *Journal of Geophysical Research*, *120*, 1329–1344. https://doi.org/10.1002/2014JB011707

Sun, T., Wang, K., & He, J. (2018). Crustal deformation following great subduction earthquakes controlled by earthquake size and mantle rheology. *Journal of Geophysical Research: Solid Earth*, *123*, 5323–5345. https://doi.org/10.1029/2017JB015242

Sun, T., Wang, K., Iinuma, T., Hino, R., He, J., Fujimoto, H., et al. (2014). Prevalence of viscoelastic relaxation after the 2011 Tohoku-oki earthquake. *Nature*, *514*(7520), 84.

Tassara, A., & Echaurren, A. (2012). Anatomy of the Andean subduction zone: Three-dimensional density model upgraded and compared against global-scale models. *Geophysical Journal International*, *189*(1), 161–168. https://doi.org/10.1111/j.1365-246X.2012.05397.x

Wang, K., Hu, Y., & He, J. (2012). Deformation cycles of subduction earthquakes in a viscoelastic Earth. *Nature*, *484*(7394), 327–332. https://doi.org/10.1038/nature11032

Wessel, P., & Smith, W. H. F. (1998). New, improved version of the generic mapping tools released. *Eos Transactions American Geophysical Union*, *79*, 579.

Wiseman, K., Bürgmann, R., Freed, A. M., & Banerjee, P. (2015). Viscoelastic relaxation in a heterogeneous Earth following the 2004 Sumatra–Andaman earthquake. *Earth and Planetary Science Letters*, *431*, 308–317. https://doi.org/10.1016/j.epsl.2015.09.024